

# Finite Element Analysis of Layered Fiber Composite Structures Accounting for the Material's Microstructure and Delamination

Bertram Stier · Jaan-Willem Simon · Stefanie Reese

Received: 10 December 2013 / Accepted: 12 December 2013 / Published online: 29 May 2014  
© Springer Science+Business Media Dordrecht 2014

**Abstract** The present paper focuses on composite structures which consist of several layers of carbon fiber reinforced plastics (CFRP). For such layered composite structures, delamination constitutes one of the major failure modes. Predicting its initiation is essential for the design of these composites. Evaluating stress-strength relation based onset criteria requires an accurate representation of the through-the-thickness stress distribution, which can be particularly delicate in the case of shell-like structures. Thus, in this paper, a solid-shell finite element formulation is utilized which allows to incorporate a fully three-dimensional material model while still being suitable for applications involving thin structures. Moreover, locking phenomena are cured by using both the EAS and the ANS concept, and numerical efficiency is ensured through reduced integration. The proposed anisotropic material model accounts for the material's micro-structure by using the concept of structural tensors. It is validated by comparison to experimental data as well as by application to numerical examples.

**Keywords** Fiber-reinforced composite · Layered composite · Delamination · Solid-shell concept · Enhanced strain formulation · Reduced integration

## 1 Introduction

Fiber-reinforced composites are gaining more and more importance in technical applications. Their most beneficial characteristics, the very high Young's modulus and low density, are particularly important for shell-like lightweight constructions. The composites examined in this paper consist of multiple layers, each of which is composed of a thermoset matrix with unidirectional fiber reinforcement.

---

B. Stier (✉) · J.-W. Simon · S. Reese  
Institute of Applied Mechanics, RWTH Aachen University, Mies-van-der-Rohe-Str. 1, 52074 Aachen,  
Germany  
e-mail: bertram.stier@rwth-aachen.de

There exist different methodologies which describe the macro-mechanical material behavior and at the same time account for the material's micro-structure. Among them, the asymptotic homogenization method for periodic structures [1–3] and the FE<sup>2</sup>-method [4–6] are prominent. As an alternative, the special character of the microstructure can be taken into account by means of an anisotropic model using the concept of structural tensors. The majority of such models formulated for finite strains were developed in the field of biomechanics. For instance, axisymmetric orthotropic blood vessels were investigated in [7], whereas biological soft tissues were modeled in [8] on the basis of an incompressible transversely isotropic law for moderate deformations.

An overview of anisotropic material models developed for reinforced fiber composites can be found e.g. in [9]. For the experimental validation of such models implemented into finite element analyses, the reader is referred to [10], while modeling techniques for layered composites including micro-macro scale transitions are presented in [11]. In the present paper, the model proposed by Reese in [12] for fiber-reinforced rubber-like composites is adopted, in which the transition from the micro-scale to the macro-scale is formulated in a general manner. This model is not restricted to rubber-like materials but also suitable for the carbon fiber-reinforced plastics (CFRP) considered here.

Structural collapse in fiber composite structures is caused by the evolution of either matrix transverse cracking, fiber fracture, or delamination. Among these different damage modes, delamination is particularly important, because it drastically reduces the bending stiffness of the structure and promotes local buckling in case of compressive loads. Including delamination into the computation of composite structures requires the definition of an appropriate criterion for its onset as well as the prediction of its growth after an initial crack has evolved. For the initiation of delamination, different criteria exist, formulated in dependence of stress-resistance relations, e.g. [13–17]. After onset of delamination, the high stress gradients appearing at the crack front prohibit the use of stress-based criteria. Thus, fracture mechanics approaches are often employed for simulating delamination propagation, such as the virtual crack closure technique, [18–22]. As an alternative, delamination growth can be treated within the framework of damage mechanics using cohesive zone models, which are incorporated into the finite element simulation by interface elements, e.g. [23–26]. In this paper, the onset of delamination is addressed by means of stress-resistance relations.

Since fiber-reinforced composites are mostly applied in thin shell-like structures, the element formulation should reproduce the thinness of the structure while at the same time three-dimensional stress states have to be displayed realistically. Although 'classical' shell formulations (e.g. with four nodes) exist which take into account the through the thickness stretching, the implementation of three-dimensional material models is much simpler in the context of solid elements. On the other hand, the latter typically show a poor performance when being applied to thin shell-like structures. In particular, there are different locking phenomena to be coped with, which cause an overestimation of the stress state and an underestimation of the deformation. Using solid-shell elements represents one strategy to overcome this problem by combining the advantages of both solid elements and shell elements at the same time. Further, applying the enhanced assumed strain (EAS) concept eliminates the volumetric locking in case of (nearly) incompressible materials as well as the Poisson thickness locking, which occurs in bending problems of shell-like structures due to the non-constant distribution of transverse normal strain over the thickness.

In the literature, one can find several solid-shell formulations incorporating the EAS concept, see e.g. [27–29], to name only a few. To cure the transverse shear locking, which is present in standard eight-node hexahedral elements, the assumed natural strain (ANS)

method is applied. the application of the ANS concept in the context of full integration formulations is discussed by e.g. [30–32].The combination of the ANS approach with reduced solid-shell formulations can be found in e.g. [33–36]. The formulation presented in this paper is based on the works of Schwarze and Reese [34–36].

For laminated layered composites, the accurate determination of the through-the-thickness stress distribution was recently investigated by several authors. For instance, in [37] an improved shell formulation was suggested for this purpose, whereas in [38] and [39] the investigations were based on the solid-shell concept. For a more elaborate literature overview, the reader is referred to the review papers [40–42] and the references therein. However, the development of solid-shell formulations, applicable to model the orthotropic behavior of thin fiber composite structures is still an open field.

## 2 Micromechanically Motivated Material Model

The fiber composites examined in this paper consist of stacked layers, each of which is composed of either unidirectional long fibers or a woven fabric embedded in a matrix material. The anisotropic material behavior of such composites is taken into account by using the micromechanically motivated model proposed by Reese [12]. In the following, the basics of the continuum model are summarized. Therein, parameters are chosen to represent approximately the behavior of carbon fibers in an epoxy resin matrix. Further, for a discussion of the theoretical background, the reader is referred to [43] and the references therein.

Introducing the deformation gradient  $\mathbf{F}$ , the deformation of a continuous body is represented by the right Cauchy-Green tensor

$$\mathbf{C} = \mathbf{F}^T \mathbf{F} \tag{1}$$

The modelling of a hyperelastic material is based on the existence of a scalar potential, which is the strain energy density function (SEDF)  $W = W(\mathbf{C})$ . The second Piola-Kirchhoff stress tensor is given by

$$\mathbf{S} = 2 \frac{\partial W(\mathbf{C})}{\partial \mathbf{C}} \tag{2}$$

In the anisotropic case considered here, the energy function  $W(\mathbf{C}, \mathbf{M}_1, \mathbf{M}_2)$  is a scalar function of  $\mathbf{C}$  and the structural tensors  $\mathbf{M}_i (i = 1, 2)$ , which are defined by

$$\mathbf{M}_i = \mathbf{n}_i \otimes \mathbf{n}_i \tag{3}$$

where the vectors  $\mathbf{n}_i$  are parallel to the fibers. Obviously, for unidirectional layers only one vector  $\mathbf{n}_1$  and one structural tensor  $\mathbf{M}_1 = \mathbf{n}_1 \otimes \mathbf{n}_1$  needs to be defined, whereas for woven composites with two families of fibers two vectors  $\mathbf{n}_1$  and  $\mathbf{n}_2$  of fiber orientation are used, as shown in Figs. 1 and 2, leading to the two structural tensors

$$\mathbf{M}_1 = \mathbf{n}_1 \otimes \mathbf{n}_1 \quad \text{and} \quad \mathbf{M}_2 = \mathbf{n}_2 \otimes \mathbf{n}_2 \tag{4}$$

Then, the SEDF can be represented in dependence of the three isotropic invariants of  $\mathbf{C}$

$$I_1 = \text{tr } \mathbf{C}, \quad I_2 = \frac{1}{2} \left[ (\text{tr } \mathbf{C})^2 - \text{tr}(\mathbf{C}^2) \right], \quad I_3 = \det \mathbf{C} \tag{5}$$

and the pseudo-invariants

$$I_k = \text{tr}(\mathbf{C} \mathbf{M}_i), \quad k = 2i + 2 \tag{6a}$$

$$I_l = \text{tr}(\mathbf{C}^2 \mathbf{M}_i), \quad l = 2i + 3 \tag{6b}$$



**Fig. 1** Representative volume element (RVE) of woven composite

The scalar product of  $\mathbf{C}$  and  $\mathbf{M}_i$ , represents the weighted square of the stretch in the direction of the corresponding structural vector. In this way, the anisotropy can be taken into account within a scalar function, when parts of the SEDF depend on the additional invariants. It is intuitively understandable, that the structural vectors are associated with the main fiber directions.

In this work, the anisotropic model of Reese [12] is adopted. In this model it is assumed that the fibers carry load only in tension. Since this assumption is not realistic for the carbon fiber reinforced plastics (CFRP) considered here, the model is slightly modified, such that the fibers can carry load also under compression. Moreover, the fiber volume fractions  $\varphi_i \geq 0$  are introduced, where  $\sum_i \varphi_i \leq 1$  holds. Except of this, we adopt the mentioned model and use the following strain energy function:

$$W = \left( 1 - \sum_{(i)} \varphi_i \right) W_{NH} + \sum_{(i)} \varphi_i W_{ani\ i} \tag{7}$$

The first part of  $W$ , representing the matrix behavior of the composite, is modeled as a Neo-Hookean material. The corresponding strain energy function reads

$$W_{NH}(I_1, I_3) = \frac{\mu}{2} (I_1 - 3) - \mu \ln \sqrt{I_3} + \frac{\Lambda}{4} (I_3 - 1 - 2 \ln \sqrt{I_3}) \tag{8}$$

where  $\mu$  and  $\Lambda$  denote the Lamé constants. The second part

$$W_{ani\ i} = \frac{1}{\alpha_i} K_i^{ani1} (I_k - 3)^{\alpha_i} + \frac{1}{\beta_i} K_i^{ani2} (I_l - 3)^{\beta_i} \tag{9}$$

is the contribution of the fibers, inducing anisotropy. In this equation  $\alpha_i, K_i^{ani1}, \beta_i$  and  $K_i^{ani2}$  are material parameters. Noticeably, in [12] further coupling terms were introduced which hardly influence the results. Therefore they are dropped here. In the special case of



**Fig. 2** Woven fibers and definition of fiber directions  $n_1$  and  $n_2$

linear behavior of the fibrous part,  $K_i^{ani1}$  can be associated with the Young's modulus of the fiber. Then  $\alpha_i = 2$  and  $K_i^{ani2} = 0$  holds.

### 3 Experimental Investigation

The data set used for validation was generated by the experimental investigation of unidirectional carbon fiber reinforced epoxy resin plates under tensile loading. Online digital image correlation (DIC) provided length change measurements at the surface of the specimens during the test procedure.

#### 3.1 Specimen

In this series, six unidirectional CFRP plates with varying fiber angles were tested. Each plate consisted of four layers of UD carbon fiber prepreg, whose specification was 'VTM264/T700SC(24K) -300-40 %RW' (Toray). Manufacturer's parameters of the used materials are itemized in Table 1.

Water jet cutting was used for manufacturing to avoid fiber and matrix damage at the plates' sides. The specimen's geometry and dimensions are given in Fig. 3 and Table 2.

Cap strips, made of the specimen's material, were applied at the plate ends to prevent fiber damage during clamping and testing. Furthermore, a random pattern was sprayed at one of the specimen sides which is needed for the DIC measurements. Titanium dioxide powder spray was used for the white base coat while graphite spray sparkles induced the contrast. Invalid tests, e.g. when slippage and/or rupture of the caps was detected, were discarded.

#### 3.2 Setup

The test setup contains a 'ZWICK Z100' testing machine and an 'ARAMIS M4' DIC system. This setup allowed for almost synchronised recording of force and displacement values. The ZWICK's load cell signal as well as the displacement signals of the (external) DIC system were recorded using the control software 'TestXpert II' of ZWICK/Roell. Analog online signal transfer — e.g. length change measured by the DIC system — from ARAMIS to the testing machines software was realized by the integration of a 'HBM Spider 8' measuring amplifier.

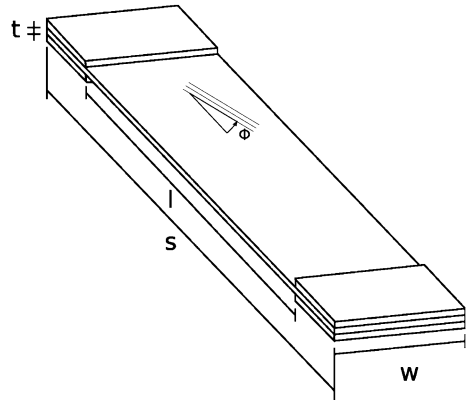
Time, force, cross beam displacement and nominal strain were generated by ZWICK's (internal) sensors. Unfortunately, the kinematic quantities were insufficient, since the deformation of the load frame and the gliding of the grippers could not be decoupled from the

**Table 1** Material parameters from manufacturer

Parameter	Fiber	Composite
Tensile modulus	230 [GPa]	135 [GPa]
Tensile strength	4900 [MPa]	2550 [MPa]
Tensile strain	2.1 %	1.7 %

Composite values normalized to 60 % fiber volume

**Fig. 3** Geometry of specimen



pure elongation of the specimen. To overcome this problem, an external displacement measurement system was applied. The ARAMIS system supported the observation of up to ten points at the specimens’ surface in the real-time-sensor (rts) mode. In this mode, ARAMIS could be seen as an optical extensometer.

Assuming a homogeneous deformation state at the center of the specimen, only two points at the longitudinal axis of the specimen were needed to determine a ‘global’ length change and strain values. Another two points at the transversal axis were observed to generate Poisson’s ratio values (Fig. 4).

### 3.3 Experimental Results

From the raw force (ZWICK) - displacement (ARAMIS) graphs of the valid measurements it could be observed, that the variation of the raw data was small over the range of applied force. Furthermore, the composite’s response was almost linear at 0°, 45°, 60°, 75° and 90° fiber angle. To the authors’ understanding, the nonlinear response at 15° and 30° was caused by the shear loading of the interphase between fiber and matrix material, that led to local debonding of the interface.

However, from the raw data it was possible to calculate the engineering stress - strain values to obtain the composites’ Young’s modulus. As mentioned before, a homogeneous deformation state and small deformations were assumed. The homogeneous strain state was confirmed by local strain field analysis. To obtain stresses, force values were divided by the plate’s initial cross-sectional area, measured before testing. The initial length was the measured distance between the two measuring points arranged along the longitudinal axis at the

**Table 2** Characteristic dimensions

Parameter	Value[mm]
s	300.0
ℓ	200.0
w	40.0
t	1.0
Fiber angles	
0° 15° 30° 45° 60° 75° 90°	

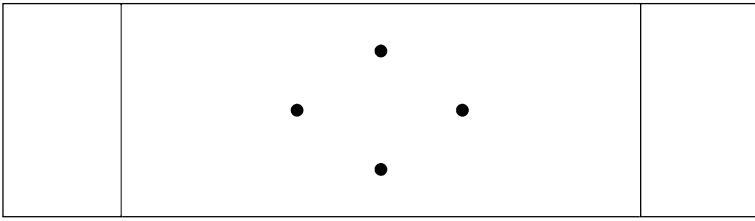


**Fig. 4** Position of measuring points for real-time-sensor (rts) mode

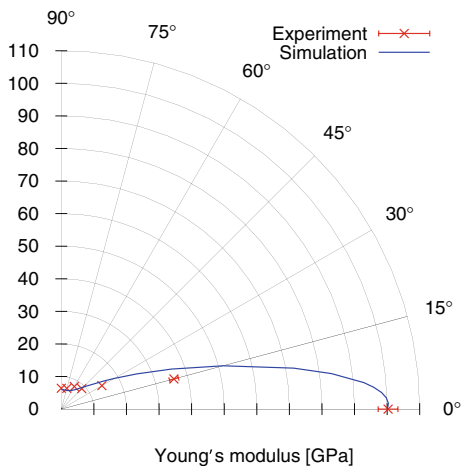
reference state. Then, the global Young’s modulus for any of the laminates was calculated by evaluating the slope of a curve, fitted to the experimental data. Since most graphs showed a linear shape, a line fitting met our purpose. The mean value and the standard deviation for every fiber angle are plotted in Fig. 5 in a polar diagram, where the typical UD-response can be seen.

**4 Validation of the Material Model**

The before mentioned material model was implemented as a user material routine within the finite element code FEAP [44]. In the simulation, the total width and thickness of the specimen were modeled with a sufficiently high number of elements. The distance of the measuring points in longitudinal direction was used as the initial length of the virtual body. Displacement boundaries of the nodes at the upper side of the virtual plate were fixed, while the displacement of the bottom nodes was equal to the experimentally measured length change. The sum of the reaction forces at the displaced nodes in longitudinal direction and the force measured during the experiments were compared.

To validate the material model, the parameters were fitted only to the 0° and 90° data. For every other angle, only the direction of the structural vector was changed. At first, the matrix material part was fitted to the 0° specimen test data, whereas the fiber part factor  $K_1^{ani1}$  was increased to suit the behaviour at 90°. The fiber volume fraction used for the simulations

**Fig. 5** Young’s modulus polar diagram: comparison of simulation and experiments



was taken from the manufacturers’ specifications. The determined material parameters are given in Table 3.

Thereby, the global Young’s modulus of the simulated composite was calculated for the different fiber orientations and plotted in the polar diagram, see Fig. 5. The simulation correlates with the experimental data, once again, showing the characteristics of UD laminate. However, at the 15° and 30° angles a slight deviation appears. This is mainly due to the fact that the linear data fit of the declining experimental data curve falls into a lower slope than initially seen, and thus, into a lower Young’s modulus. Nevertheless, the validation of the material model is highly satisfactory.

### 5 Delamination Onset Criterion

The onset of delamination can be determined on the basis of stress-strength relations. In particular, delamination occurs in pure interlaminar tension (mode I), pure interlaminar sliding shear (mode II), and pure interlaminar scissoring shear (mode III), if the corresponding interlaminar stress component exceeds the respective maximum interfacial strength. Here, the interlaminar stress components are denoted by  $\sigma_{13}$ ,  $\sigma_{23}$ , and  $\sigma_{33}$ , respectively, where the 3-direction is normal to the considered interface. Then, the respective interfacial strengths are  $Z_{13}$ ,  $Z_{23}$ , and  $Z_{33}$ .

To account for mixed-mode loading, the formulation of the onset criterion should incorporate the interaction of these modes. Due to the lack of available experimental data, failure criteria predicting the initiation of delamination have not been fully validated, and hence only few formulations exist. In this paper, the approach of Ye [14] is adopted, in which a quadratic interaction of modes is assumed:

$$\text{if } \sigma_{33} > 0 : \quad \left(\frac{\sigma_{33}}{Z_{33}}\right)^2 + \left(\frac{\sigma_{31}}{Z_{31}}\right)^2 + \left(\frac{\sigma_{32}}{Z_{32}}\right)^2 \geq 1 \quad (10a)$$

$$\text{if } \sigma_{33} \leq 0 : \quad \left(\frac{\sigma_{31}}{Z_{31}}\right)^2 + \left(\frac{\sigma_{32}}{Z_{32}}\right)^2 \geq 1 \quad (10b)$$

As the formulation presented in this paper is capable of taking into account finite strains, it is important to accurately represent the corresponding stress components. First of all, the stresses calculated by the present solid-shell formulation are expressed by the second Piola-Kirchhoff stress tensor  $\mathbf{S}$ , which has to be pushed to the current configuration

$$\boldsymbol{\sigma} = \frac{1}{\det \mathbf{F}} \mathbf{F} \mathbf{S} \mathbf{F}^T \quad (11)$$

where  $\boldsymbol{\sigma}$  denotes the Cauchy stress tensor. From this, using Cauchy’s theorem  $\mathbf{t} = \boldsymbol{\sigma} \mathbf{n}$ , the interlaminar traction  $\sigma_n$  and the interlaminar resultant shear  $\tau_n$  can be achieved by

$$\sigma_n = \mathbf{n} \boldsymbol{\sigma} \mathbf{n} \quad (12)$$

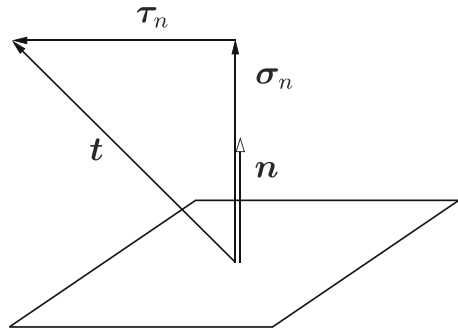
$$\tau_n = \sqrt{||\mathbf{n} \boldsymbol{\sigma} ||^2 - \sigma_n^2} \quad (13)$$

**Table 3** Parameter set (non-zero values)

Parameter	$\varphi_1$	$\Lambda$	$\mu$	$K_1^{ani1}$	$\alpha_1$
Value	0.4	2900	17000	210000	2



**Fig. 6** Traction vectors acting on infinitesimal surface element



denoting the normal vector of the considered interface by  $\mathbf{n}$ , see Fig. 6. For consistency, the maximum interfacial strength in tension and resultant shear are referred to as  $Z_\sigma$  and  $Z_\tau = \sqrt{Z_{31}^2 + Z_{32}^2}$ , respectively. Consequently, the condition for delamination onset reads:

$$\text{if } \sigma_n > 0 : \quad \left(\frac{\sigma_n}{Z_\sigma}\right)^2 + \left(\frac{\tau_n}{Z_\tau}\right)^2 \geq 1 \quad (14a)$$

$$\text{if } \sigma_n \leq 0 : \quad \left(\frac{\tau_n}{Z_\tau}\right)^2 \geq 1 \quad (14b)$$

This condition has to be checked in each loading step and in each interface of the laminated composite. Thus, the accurate prediction of the stress components in the interfaces is essential for a reliable prediction of the initiation of debonding. Since the layers are usually rather thin, solid elements are not suitable to achieve sufficient accuracy. To overcome this problem, spline approximations for the through-the-thickness stresses can be applied, as proposed in [16]. Even so, using solid elements in the thin shell-like applications should be avoided, and solid-shell elements are preferable.

Further, it should be noticed that this kind of criterion is suitable to predict the delamination onset, but delamination growth is not covered.

### 6 Solid-Shell formulation

Using standard solid elements in thin structures would require a very high mesh density to predict the stress distribution with sufficient accuracy. Hence, the solid-shell element formulation is used as an alternative to avoid inefficient computations. Furthermore, the different locking phenomena are cured by application of the EAS and ANS concepts. The following derivation is based on the works of Schwarze and Reese [34–36].

The solid-shell concept is based on the two-field variational functional

$$g_1(\mathbf{u}, \mathbf{E}_e) = \int_{B_0} \mathbf{S}(\mathbf{E}) : \delta \mathbf{E}_c \, dV + g_{\text{ext}} = 0 \quad (15)$$

$$g_2(\mathbf{u}, \mathbf{E}_e) = \int_{B_0} \mathbf{S}(\mathbf{E}) : \delta \mathbf{E}_e \, dV = 0 \quad (16)$$

where  $g_{\text{ext}}$  denotes the virtual work of the external loading. For this formulation, the total Green-Lagrange strain tensor  $\mathbf{E}$  is split additively into the compatible part  $\mathbf{E}_c$  and the enhanced part  $\mathbf{E}_e$  coming from the EAS concept:

$$\mathbf{E} = \mathbf{E}_c + \mathbf{E}_e \tag{17}$$

In this work, isoparametric eight-node hexahedral finite elements are considered, such that both the position vector of the reference configuration  $\mathbf{X}(\boldsymbol{\xi}) = [X_1, X_2, X_3]^T$  and the displacement vector  $\mathbf{U}(\boldsymbol{\xi}) = [\mathbf{U}_1, \mathbf{U}_2, \mathbf{U}_3]^T$  are approximated within the element by

$$X_i = \sum_{I=1}^8 N_I X_{iI} \quad \text{and} \quad U_i = \sum_{I=1}^8 N_I U_{iI} \quad (i = 1, 2, 3) \tag{18}$$

using tri-linear shape functions

$$N_I = 1/8(1 + \xi_I \xi)(1 + \eta_I \eta)(1 + \zeta_I \zeta) \quad (I = 1, \dots, 8) \tag{19}$$

The position vector of the current (deformed) configuration reads

$$\mathbf{x}(\boldsymbol{\xi}) = \mathbf{X}(\boldsymbol{\xi}) + \mathbf{U}(\boldsymbol{\xi}) \tag{20}$$

Then, introducing  $\mathbf{D} = \partial \mathbf{U} / \partial \boldsymbol{\xi}$ , the Jacobian matrices  $\mathbf{J}$  and  $\tilde{\mathbf{J}}$  of the reference and the current configuration, respectively, can be written as follows:

$$\mathbf{J} = \frac{\partial \mathbf{X}}{\partial \boldsymbol{\xi}} = [\mathbf{J}_1, \mathbf{J}_2, \mathbf{J}_3] \quad \text{and} \quad \tilde{\mathbf{J}} = \frac{\partial \mathbf{x}}{\partial \boldsymbol{\xi}} = \mathbf{J} + \mathbf{D} = [\tilde{\mathbf{J}}_1, \tilde{\mathbf{J}}_2, \tilde{\mathbf{J}}_3] \tag{21}$$

The columns of  $\mathbf{J}$  and  $\tilde{\mathbf{J}}$  represent the covariant base vectors with respect to the reference and current configuration, respectively. The contravariant base vectors with respect to the initial configuration and the current configuration are denoted by

$$\mathbf{H}_i = \frac{\partial \xi_i}{\partial X_j} \mathbf{e}_j = j_{ij} \mathbf{e}_j \quad \text{and} \quad \tilde{\mathbf{H}}_i = \frac{\partial \xi_i}{\partial x_j} \mathbf{e}_j = \tilde{j}_{ij} \mathbf{e}_j \tag{22}$$

These represent the rows of the inverse Jacobian matrices  $\mathbf{J}^{-1}$  and  $\tilde{\mathbf{J}}^{-1}$ , respectively, the coefficients of which are denoted by  $j_{ij} = (\mathbf{J}^{-1})_{ij}$  and  $\tilde{j}_{ij} = (\tilde{\mathbf{J}}^{-1})_{ij}$ . With this definition, the Green-Lagrange strain tensor can be written in terms of its Cartesian and covariant components  $E_{ij}$  and  $\bar{E}_{ij} = E_{\xi_i \xi_j}$ , respectively,

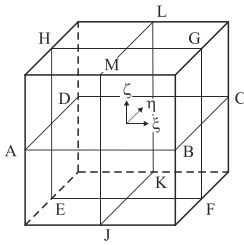
$$\mathbf{E} = E_{ij} \mathbf{e}_i \otimes \mathbf{e}_j = \bar{E}_{ij} \mathbf{H}_i \otimes \mathbf{H}_j \tag{23}$$

Denoting the Voigt notation by  $(\bullet)$  and exploiting symmetry as well as  $\Gamma_{ij} = 2 E_{ij}$ , the latter can be stored into the  $6 \times 1$  vectors

$$\hat{\mathbf{E}} = \{E_{11}, E_{22}, E_{33}, \Gamma_{12}, \Gamma_{23}, \Gamma_{13}\}^T \tag{24}$$

$$\hat{\bar{\mathbf{E}}} = \{E_{\xi\xi}, E_{\eta\eta}, E_{\zeta\zeta}, \Gamma_{\xi\eta}, \Gamma_{\eta\zeta}, \Gamma_{\xi\zeta}\}^T \tag{25}$$

These can be transformed one to the other with the relation  $\hat{\bar{\mathbf{E}}} = \mathbf{T} \hat{\mathbf{E}}$ , where  $\mathbf{T}$  is a transformation matrix which depends on the coefficients  $j_{ij}$ . Consequently, the compatible Green-Lagrange strain is written in the form  $\hat{\mathbf{E}}_c = \mathbf{T} \hat{\bar{\mathbf{E}}}_c$ . To cure curvature thickness locking, the ANS concept is implemented. For this, the covariant compatible strain terms  $E_{c \zeta \zeta} |_{\xi \mathbf{K}} := E_{c \zeta \zeta}^{\mathbf{K}}$  are evaluated at the sampling points  $\mathbf{K} = A, \dots, D$ , see Fig. 7, as proposed in [45].



$$\begin{aligned}
 \xi_A &= (-1, -1, 0)^T & \xi_E &= (-1, 0, -1)^T & \xi_J &= (0, -1, -1)^T \\
 \xi_B &= (1, -1, 0)^T & \xi_F &= (1, 0, -1)^T & \xi_K &= (0, 1, -1)^T \\
 \xi_C &= (1, 1, 0)^T & \xi_G &= (1, 0, 1)^T & \xi_L &= (0, 1, 1)^T \\
 \xi_D &= (-1, 1, 0)^T & \xi_H &= (-1, 0, 1)^T & \xi_M &= (0, -1, 1)^T
 \end{aligned}$$

Fig. 7 Sampling points of the ANS concept at reference element

Thereby, the covariant compatible strains can be interpolated within the shell mid plane of the reference element by means of bilinear ansatz functions

$$\bar{N}_K = 1/4(1 + \xi_K \xi)(1 + \eta_K \eta) \tag{26}$$

to be evaluated in the points  $K = A, \dots, D$ . In consequence, the assumed transverse normal strain distribution reads

$$E_{c\zeta\zeta}^{ANS} = \bar{N}_A E_{c\zeta\zeta}^A + \bar{N}_B E_{c\zeta\zeta}^B + \bar{N}_C E_{c\zeta\zeta}^C + \bar{N}_D E_{c\zeta\zeta}^D = \sum_{K=A}^D \bar{N}_K E_{c\zeta\zeta}^K \tag{27}$$

In order to overcome the transverse shear locking, following [33], four sampling points  $K = E, \dots, H$  are used for the transverse shear term  $\Gamma_{c\eta\zeta}|_{\xi_K} := \Gamma_{c\eta\zeta}^K$  and  $K = J, \dots, M$  for  $\Gamma_{c\xi\zeta}|_{\xi_K} := \Gamma_{c\xi\zeta}^K$ , see again Fig. 7. Using the ansatz functions (26) for the respective points, the assumed transverse shear terms read

$$\Gamma_{c\eta\zeta}^{ANS} = \sum_{K=E}^H \bar{N}_K \Gamma_{c\eta\zeta}^K \quad \text{and} \quad \Gamma_{c\xi\zeta}^{ANS} = \sum_{K=J}^M \bar{N}_K \Gamma_{c\xi\zeta}^K \tag{28}$$

The present solid-shell formulation utilizes a reduced integration scheme within the shell plane (using one integration point), whereas a full integration is used in thickness direction, which allows for choosing arbitrary numbers of integration points (at least two), see Fig. 8. Thus, all integration points are located on the normal through the center of the element defined by  $\xi^* := (0, 0, \zeta)^T$ .

To cure volumetric locking as well as Poisson thickness locking, the EAS concept is adopted. These locking effects are treated on the level of the integration points, which can be expressed by  $\hat{E}_e = \hat{E}_e^*$ , indicating values to be evaluated in the integration points by  $*$ . Since in (27) the assumed transverse normal strain  $E_{e\zeta\zeta}^{ANS}$  has been defined independently of  $\zeta$ , the according value  $E_{e\zeta\zeta}$  is constructed as being linear in  $\zeta$  in order to overcome the locking effects, which reads

$$\hat{E}_e = \hat{E}_e^* = T^0 \bar{B}_e^* W_e \tag{29}$$

Fig. 8 Sketch of the fastened joint

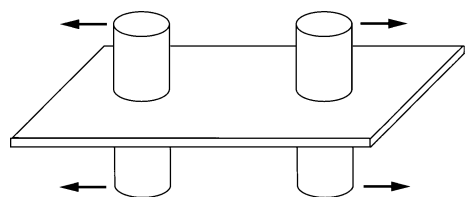
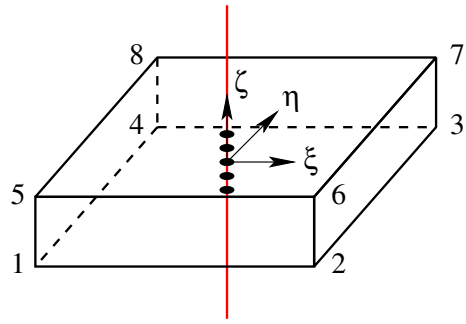


**Fig. 9** Solid-shell element with integration points at  $\xi = \xi^* := (0, 0, \zeta)^T$



in which the interpolation matrix  $\bar{\mathbf{B}}_e^* = [0, 0, \zeta, 0, 0, 0]^T$  requires only one EAS degree-of-freedom  $W_e$ . Here,  $\mathbf{T}^0$  is the transformation matrix evaluated in the center of the element.

Concluding, the solid-shell element used in this paper is efficient due to the use of reduced integration. Stability is achieved by means of a suitable hourglass stabilization. For further details, the reader is referred to the works of Schwarze and Reese [34–36]. Since the number of integration points over the thickness can be arbitrarily chosen, the element is predestinated for the computation of thin layered structures where the fully three-dimensional material behaviour plays an important role.

## 7 Numerical Examples

### 7.1 Mechanically Fastened Joint

For validation, the proposed method is applied to a mechanically fastened joint in a composite sheet consisting of 8 layers in a symmetric assembly  $(0^\circ, 90^\circ, +45^\circ, -45^\circ)_s$ , each of which is made of unidirectional CFRP (*Hexel T300/914*). The length of the sheet is 200 mm, the height 2 mm, the width 36 mm. It contains two circular holes of diameter 6 mm, which are located at a distance of 36 mm from the end of the sheet, measured from the hole’s center. In each of the holes, a very stiff tight-fitting bolt is placed and moved in longitudinal outward direction of the sheet, as shown schematically in Fig. 9, applying 0.01 mm displacement per time step.

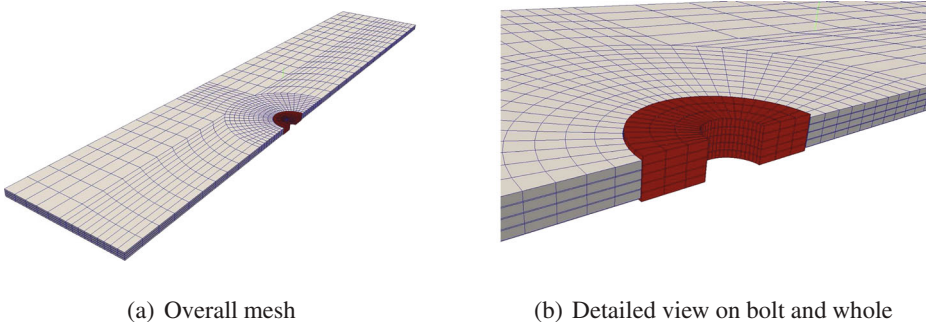


**Fig. 10** Mesh of the fastened joint

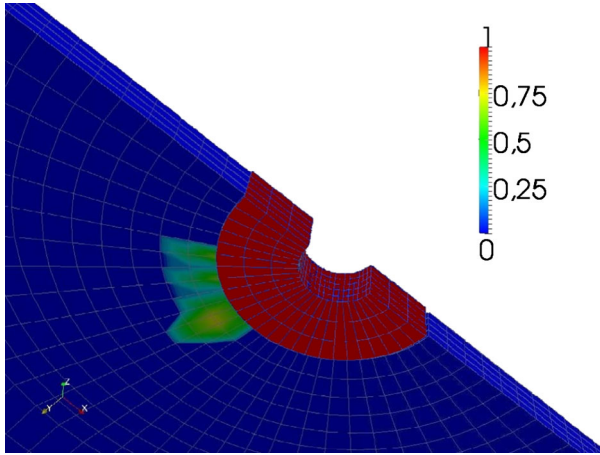


**Fig. 11** Resulting zone of delamination onset

Due to the symmetry of the system, only one eighth of the sheet is considered in the computation (see Fig. 10a), applying symmetric boundary conditions. In addition, the elements at the upper surface surrounding the hole are fixed in thickness direction to simulate a finger-tight washer. In order to incorporate delamination, interface elements are located between all layers, with only matrix material properties assigned. The latter are assumed to be ten times thinner than the layers. Whereas the described solid-shell element is used for both layers and interfaces –leading to a total number of 5800 solid-shell elements with 7164 nodes– the bolt is discretized by 375 hexahedral solid elements with 624 nodes (see Fig. 10b).

In order to compare the results with the ones obtained in [16], the material parameters given therein are used. The parameters for the carbon fibers –taken from the Torayca T300 data sheet– and the epoxy matrix –taken from the HexPly 914 product data– are given in Table 4. In addition, the values for the interfacial strengths are given as reported in [16].

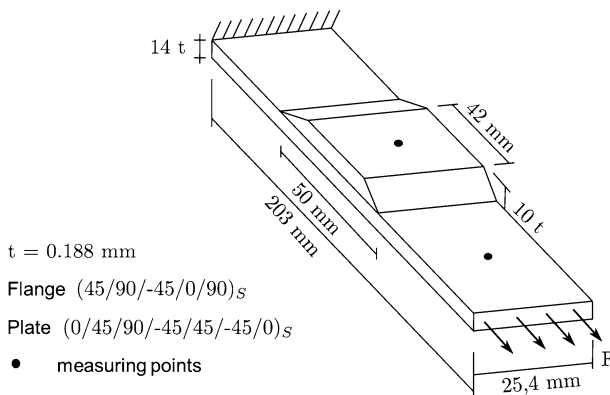


**Fig. 12** Geometry and setup of the panel

**Table 4** Material properties

Tensile modulus fiber [GPa]	230
Tensile modulus matrix [GPa]	3.9
Calc. shear modulus matrix [GPa]	1.4
Poisson's ratio matrix	0.41
Interfacial traction strength $Z_\sigma = Z_{33}$ [MPa]	76
Interfacial shear strength $Z_{31} = Z_{32}$ [MPa]	79
Interfacial resultant shear strength $Z_\tau$ [MPa]	$79\sqrt{2}$

Thereby, the non-zero parameters for the described model are computed as follows, taking into account the fiber volume fraction  $\varphi_1 = 60\%$ ;

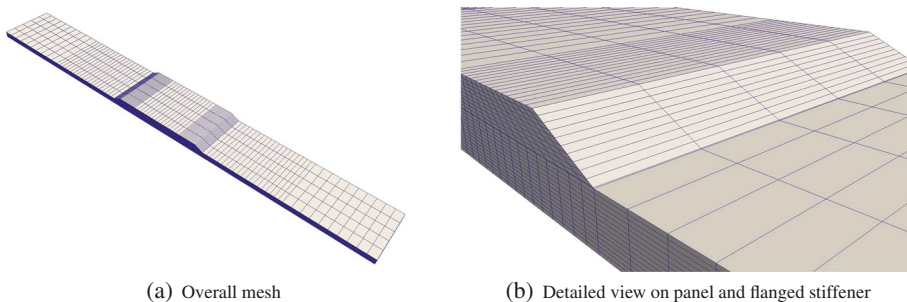
$$\Lambda = 6300 \text{ MPa}, \quad \mu = 1383 \text{ MPa}, \quad K_1^{ani1} = 1.15 \times 10^5 \text{ MPa}, \quad \alpha_1 = 2 \quad (30)$$

The location of delamination initiation is shown in Fig. 11, which corresponds to the deformation state, where the delamination onset condition is exceeded first. Delamination occurs at first close to the boundary of the hole in the lower surface of the model, which is the middle surface of the sheet. The location of delamination is reasonable and in agreement with the results presented in [16]. Furthermore, experimental data for this problem can be found in [46]. Therein, the cross head displacement corresponding to delamination onset is approximately given by 1.15 mm, whereas in the current calculation, the delamination initiates after time step with 1.2 mm.

## 7.2 Panel with Co-cured Stiffener

As a second example, the proposed method was applied to a panel with a co-cured stiffener, which had already been investigated in [17]. The panel's length and width were 203 mm and 25.4 mm, respectively, while the stiffener's length was 50 mm at the panel's skin and 42 mm at the uppermost layer, see Fig. 12. The flange was composed of 10 plies with a lay-up of  $(45^\circ/90^\circ/-45^\circ/0^\circ/90^\circ)_s$ , whereas the panel consisted of 14 plies with an  $(0^\circ/45^\circ/90^\circ/-45^\circ/45^\circ/-45^\circ/0^\circ)_s$  assembly.

All layers were made of unidirectional CFRP, the properties of which are the same as in the previous example (see Table 4) except for the fiber volume fraction  $\varphi_1 = 62\%$ . The panel was clamped at the left end, while it was loaded by a force in longitudinal direction at its right end. Since the onset of debonding was expected at the tip of the stiffener flange,

**Fig. 13** Mesh of the stiffened panel

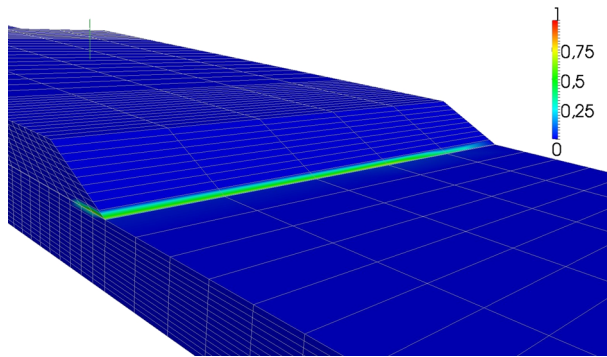


**Fig. 14** Resulting zone of delamination onset

the mesh was refined in this region as illustrated in Fig. 13a and b. In order to incorporate delamination, interface elements were located between all layers, which were furnished with material properties of the matrix alone. The latter were assumed to be ten times thinner than the layers. The described solid-shell element was used for both layers and interfaces, leading to a total number of 9825 solid-shell elements with 25152 nodes.

The location of delamination initiation is shown in Fig. 14, which corresponds to the time step, in which the delamination onset condition was met first. Delamination occurred at first at the tip of the stiffener flange, as was expected. This location of delamination is reasonable and in agreement with the results presented in [17].

In addition, experimental data for this problem are provided in [17]. Therein, the maximum displacements from extensometer measurements corresponding to delamination onset are reported to be in the range of 0.11 mm to 0.15 mm. Unfortunately, the exact location of the measurement points is not given, which does not allow a quantitative comparison. However, in the current calculation, the computed displacements at delamination onset are in a higher range up to 0.18 mm. This difference can be explained by the fact that residual stresses are present in the specimens due to the manufacturing process, which were not taken into account in the present calculation.

## 8 Conclusion

For many technical applications of fiber-reinforced composites, predicting the onset of delamination is essential for appropriately designing the considered structure. For this, a delamination onset criterion based on stress-strength relations has been suggested in this paper, which requires an accurate representation of the through-the-thickness stress distribution. The proposed solid-shell element is particularly suitable to achieve the required accuracy especially in the thin shell-like applications considered here. The formulation allows for including either unidirectional long fibers or woven fabrics with two different families of fibers, incorporating a fully three-dimensional, anisotropic, micromechanically motivated material model, which has been validated experimentally. Concluding, the proposed method is capable of predicting the initiation of delamination of fiber-reinforced composites in shell-like structures.

## References

1. Ladeveze, P., Nouy, A.: On a multiscale computational strategy with time and space homogenization for structural mechanics. *Comput. Methods Appl. Mech. Eng.* **192**, 3061–3087 (2003)
2. Kouznetsova, V.G., Geers, M.G.D., Brekelmans, W.A.M.: Multiscale second order computational homogenization of multi-phase materials: a nested finite element strategy. *Comput. Methods Appl. Mech. Eng.* **193**, 5525–5550 (2004)
3. Violeau, D., Ladeveze, P., Lubineau, G.: Micromodel-based simulations for laminated composites. *Compos. Sci. Technol.* **69**(9), 1364–1371 (2009)
4. Zienkiewicz, O.C., Taylor, R.L.: *The Finite Element Method for Solid and Structural Mechanics*, 6th edn. Elsevier, Amsterdam (2005)
5. Kanoute, P., Boso, D.P., Chaboche, J.L., Schrefler, B.A.: Multiscale methods for composites: a review. *Arch. Comput. Methods Eng.* **16**, 31–75 (2009)
6. Klusemann, B., Svendsen, B.: Homogenization modeling of thin-layer-type microstructure. *Int. J. Solids Struct.* **49**(13), 1828–1838 (2012)
7. Holzapfel, G.A.: Determination of material models for arterial walls from uniaxial extension tests and histological structure. *J. Theor. Biol.* **238**, 290–302 (2006)
8. Gasser, T.C., Ogden, R.W., Holzapfel, G.A.: Hyperelastic modelling of arterial layers with distributed collagen fibre orientations. *J. Royal Soc. Interface* **3**, 15–35 (2006)
9. Ansar, M., Xinwei, W., Chouwei, Z.: Modeling strategies of 3D woven composites: a review. *Compos. Struct.* **93**(8), 1947–1963 (2011)
10. Lomov, S., Ivanov, D., Verpoest, I., et al.: Full-field strain measurements for validation of meso-FE analysis of textile composites. *Compos. Part A* **39**(8), 1218–1231 (2008)
11. Toledo, M., Nallim, L., Luccioni, B.: A micro-macromechanical approach for composite laminates. *Mech. Mater.* **40**(11), 885–906 (2008)
12. Reese, S.: Meso-macro modelling of fiber-reinforced rubber-like composites exhibiting large elastoplastic deformation. *Int. J. Solids Struct.* **40**, 951–980 (2003)
13. Hashin, Z., Rotem, A.: A fatigue failure criterion for fiber reinforced materials. *J. Compos. Mater.* **7**, 448–464 (1973)
14. Ye, L.: Role of matrix resin in delamination onset and growth in composite laminates. *Compos. Sci. Technol.* **33**(4), 257–277 (1988)
15. Davila, C.G., Johnson, E.R.: Analysis of delamination initiation in postbuckled dropped-ply laminates. *AIAA J.* **31**, 721–727 (1993)
16. Camanho, P.P., Matthews, F.L.: Delamination onset prediction in mechanically fastened joints. *J. Compos. Mater.* **33**, 906–927 (1999)
17. Turon, A., Camanho, P.P., Costa, J., Davila, C.G.: A damage model for the simulation of delamination in advanced composites under variable-mode loading. *Mech. Mater.* **38**, 1072–1089 (2006)
18. O'Brien, T.K.: Interlaminar fracture toughness: the long and winding road to standardization. *Compos. Part B* **29**(1), 57–62 (1998)
19. Liu, S.: Quasi-impact damage initiation and growth of thick-section and toughened composite materials. *Int. J. Solids Struct.* **31**, 3079–3098 (1999)
20. Zou, Z., Reid, S.R., Li, S., Soden, P.D.: Modelling interlaminar and intralaminar damage in filament wound pipes under quasi-static indentation. *J. Compos. Mater.* **36**, 477–499 (2002)
21. Tay, T.: Characterization and analysis of delamination fracture in composites: an overview of developments from 1990 to 2001. *Appl. Mech. Rev.* **56**(1), 1–32 (2003)
22. Krueger, R.: Virtual crack closure technique: history, approach, and applications. *Appl. Mech. Rev.* **57**(2), 109–143 (2004)
23. de Borst, R., Remmers, J.J.C.: Computational modelling of delamination. *Compos. Sci. Technol.* **66**, 713–722 (2006)
24. Balzani, C., Wagner, W.: An interface element for the simulation of delamination in unidirectional fiber-reinforced composite laminates. *Eng. Fract. Mech.* **75**, 2597–2615 (2008)
25. Cid Alfaro, M.V., Suiker, A.S.J., de Borst, R., Remmers, J.J.C.: Analysis of fracture and delamination in laminates using 3D numerical modelling. *Eng. Fract. Mech.* **76**, 761–780 (2009)
26. Whang, C., Zhang, H., Shi, G.: 3D Finite element simulation of impact damage of laminated plates using solid-shell interface elements. *Appl. Mech. Mater.* **130–134**, 766–770 (2012)
27. Valente, R., Alves de Sousa, R., Natal Jorge, R.: An enhanced strain 3D element for large deformation elastoplastic thin shell applications. *Comput. Mech.* **34**, 38–52 (2004)



28. Alves de Sousa, R., Cardoso, R., Valente, R., Yoon, J., Gracio, J., Natal Jorge, R.: A new one-point quadrature enhanced assumed strain (EAS) solid shell element with multiple integration points along thickness—Part II: nonlinear applications. *Int. J. Numer. Methods Eng.* **67**, 160–188 (2006)
29. Reese, S.: A large deformation solid-shell concept based on reduced integration with hourglass stabilization. *Int. J. Numer. Methods Eng.* **69**, 1671–1716 (2007)
30. Tan, X., Vu-Quoc, L.: Efficient and accurate multilayer solid-shell element: non-linear materials at finite strain. *Int. J. Numer. Methods Eng.* **63**, 2124–2170 (2005)
31. Kim, K., Liu, G., Han, S.: A resultant 8-node solid-shell element for geometrically nonlinear analysis. *Comput. Mech.* **35**, 315–331 (2005)
32. Klinkel, S., Gruttmann, F., Wagner, W.: A robust nonlinear solid-shell element based on a mixed variational formulation. *Comput. Methods Appl. Mech. Eng.* **195**, 179–201 (2006)
33. Cardoso, R., Yoon, J., Mahardika, M., Choudhry, S., Alves de Sousa, R., Valente, R.: Enhanced assumed strain (EAS) and assumed natural strain (ANS) methods for one-point quadrature solid-shell elements. *Int. J. Numer. Methods Eng.* **75**, 156–187 (2008)
34. Schwarze, M., Reese, S.: A reduced integration solid-shell element based on the EAS and the ANS concept—geometrically linear problems. *Int. J. Numer. Methods Eng.* **80**, 1322–1355 (2009)
35. Schwarze, M., Vladimirov, I., Reese, S.: Sheet metal forming and springback simulation by means of a new reduced integration solid-shell finite element technology. *Comput. Methods Appl. Mech. Eng.* **200**, 454–476 (2011)
36. Schwarze, M., Reese, S.: A reduced integration solid-shell finite element based on the EAS and the ANS concept - large deformation problems. *Int. J. Numer. Methods Eng.* **85**, 289–329 (2011)
37. Roy, T., Manikandan, P., Chakraborty, D.: Improved shell finite element for piezothermoelastic analysis of smart fiber reinforced composite structures. *Finite Elem. Anal. Des.* **46**(9), 710–720 (2010)
38. Yao, L.-Q., Lu, L.: An electric node concept for solid-shell elements for laminate composite piezoelectric structures. *ASME J. Appl. Mech.* **72**, 35–43 (2005)
39. Moreira, R., Alves de Sousa, R., Valente, R.: A solid-shell layerwise finite element for non-linear geometric and material analysis. *Compos. Struct.* **92**(6), 1517–1523 (2010)
40. Rah, K., Van Paepegem, W., Habraken, A., Alves de Sousa, R., Valente, R.: Evaluation of different advanced finite element concepts for detailed stress analysis of laminated composite structures. *Int. J. Mater. Form.* **2**(1), 943–947 (2009)
41. Liu, P., Zheng, J.: Recent developments on damage modeling and finite element analysis for composite laminates: a review. *Mater. Design* **31**(8), 3825–3834 (2010)
42. Kreja, I.: A literature review on computational models for laminated composite and sandwich panels. *Cent. Eur. J. Eng.* **1**(1), 59–80 (2011)
43. Svendsen, B.: On the representation of constitutive relations using structure tensors. *Int. J. Eng. Sci.* **32**, 1889–1892 (1994)
44. FEAP 8.3: University of California. [www.ce.berkeley.edu/feap](http://www.ce.berkeley.edu/feap) (2011)
45. Bischoff, M., Ramm, E.: Shear deformable shell elements for large strains and rotations. *Int. J. Numer. Methods Eng.* **40**, 4427–4449 (1997)
46. Camanho, P.P., Bowron, S., Matthews, F.L.: Failure mechanisms in bolted CFRP. *J. Reinf. Plast. Compos.* **17**(3), 205–233 (1998)